PAPER • OPEN ACCESS

A drill-integrated miniaturized device for detecting ice in lunar regolith: the PROSPECT permittivity sensor

To cite this article: R Trautner *et al* 2021 *Meas. Sci. Technol.* **32** 125117

View the article online for updates and enhancements.

A drill-integrated miniaturized device for detecting ice in lunar regolith: the PROSPECT permittivity sensor

R Trautner[1,*] , P Reiss[1] and G Kargl[2]

[1] European Space Research and Technology Centre, European Space Agency, Noordwijk, The Netherlands
[2] Space Research Institute, Austrian Academy of Sciences, Graz, Austria

E-mail: roland.trautner@esa.int

Abstract

The detection and characterization of lunar resources, including water ice, is a key area of interest for a new generation of lunar missions. The electrical properties of water ice in the extremely low frequency range support its detection by means of *in-situ* permittivity measurements. A new type of miniaturized subsurface permittivity sensor is presented, which is under development for the PROSPECT package on the Luna-27 lander mission. Here, the sensor concept is described, key design features are presented and possible operations modes are introduced. The expected accuracy for measurements of the relative permittivity along the borehole is ∼10–15% and depends mainly on the accuracy of borehole geometry models. Laboratory test results from a prototype sensor on a water ice/simulant mixture at cryogenic temperatures are presented, demonstrating the capability to detect water ice at 125 K. The improved capabilities of the flight design are discussed, operational modes are explained and alternative electrode configurations for lunar landers and rovers are proposed.

Keywords: Moon exploration, permittivity sensor, lunar water, *in-situ* measurement

(Some figures may appear in colour only in the online journal)

1. Introduction

1.1. Background

The identification and utilization of lunar resources such as water ice has become part of the focal areas of a new generation of lunar missions. Spacecraft like the Lunar Reconnaissance Orbiter (LRO) (Spudis *et al* 2013) provided evidence for lunar water, predominantly present in permanently shaded polar regions. The LCROSS impact in Cabeus crater (Colaprete *et al* 2010) provided ground truth at that specific location, indicating a water content of 5.6 ± 2.9% by mass present in the impact ejecta. In particular, the lunar polar areas are thought to harbor significant amounts of water ice, which are of considerable interest for both science and exploration. Prospecting for lunar ice resources requires suitable sensing methods that can operate reliably in the harsh lunar environment. Desired instrument properties for space applications typically include small size and mass, low power consumption, wide non-operational/operational temperature range and low complexity.

The PROSPECT package (Trautner *et al* 2018), which is scheduled for launch in 2025 aboard the Russian Luna-27 mission to the lunar south pole region, includes a miniaturized sensor for measuring the dielectric constant of lunar subsurface materials by means of low frequency alternating currents injected into the regolith. Water ice shows a distinctive

signature in the frequency domain especially at extremely low frequency (ELF), and can be detected and quantified via the measurement of the dielectric properties of lunar soil. The ProSPA laboratory that is part of PROSPECT will determine the volatile content of a sample taken from a certain depth via evolved gas analysis. The measurement of the subsurface dielectric constant supports the interpretation of this gas analysis data, as it helps to estimate sample mass, compaction and ice quantity using relationships derived from Apollo sample analysis. The PROSPECT permittivity sensor presented here draws from heritage of past instruments, including permittivity probes on Huygens (Ferri *et al* 2002), Rosetta Philae (Seidensticker *et al* 2007), and early subsurface permittivity sensor prototypes (Trautner *et al* 2004). Its miniaturized design enables the integration in the ProSEED drill rod of PROSPECT that is used to acquire subsurface samples from down to 1 m depth.

1.2. Electrical and physical properties of lunar regolith

The lunar surface is covered by a fragmental layer of broken, melted, and otherwise altered rock material called regolith. The bulk of this regolith consists of small particles <1 cm in size (McKay *et al* 1991), which can generally be referred to as soil. A fraction of larger pebbles or cobbles may be embedded in the soil. The electrical properties of the lunar surface materials are those of silicates, characterized by extremely low loss and low electrical conductivity. In the total absence of water, the DC electrical conductivity ranges from 10^{-14} mho m^{-1} for lunar soils to 10^{-9} mho m^{-1} for lunar rocks at 300 K in darkness. The relative dielectric permittivity ε_r for lunar materials is approximately

$$\varepsilon_r = 1.9^{\rho} \tag{1}$$

where ρ represents the bulk density in g cm^{-3}. The relative dielectric permittivity is dominantly controlled by bulk density and is independent of chemical or mineralogical composition (Carrier *et al* 1991). Analysis of Apollo samples has shown that lunar soils and rocks typically exhibit a different range of dielectric constant. Using the relationship

$$\rho = 1.92 \frac{z + 12.2}{z + 18} \tag{2}$$

where z is the depth in cm (Carrier *et al* 1991), we obtain $\varepsilon_r = 2.51$ for a near-surface density of 1.44 g cm^{-3} at 5 cm depth to $\varepsilon_r = 3.23$ for a bulk density of 1.83 g cm^{-3} at the maximum PROSPECT drilling depth of 100 cm. Lunar rocks on the other hand exhibit a dielectric constant of $\varepsilon_r = 4$ and higher (Olhoeft and Strangway 1975) and at the same time have a significantly higher conductivity.

From an electrical point of view, dry lunar regolith can be represented by an excellent isolator of moderate dielectric constant, with a small fraction of embedded bodies of a size larger than a few millimeters, that exhibit a higher dielectric constant and a significantly higher conductivity.

An *in-situ* measurement of the dielectric constant along the wall of a borehole can therefore be expected to allow

determination of the soil density over depth, and observed local enhancements of the complex permittivity should allow to infer the presence of subsurface rocks or rock fragments.

The presence of water ice significantly alters the electrical properties of lunar regolith. In pure form, ice exhibits a high dielectric constant with a pronounced ELF frequency response that is highly dependent on temperature (Petrenko and Whitworth 2002). In mixture with lunar regolith simulants the dielectric constant is lower than with real lunar regolith but still shows the characteristic response over both frequency and temperature. Experiments with mixtures of lunar soil simulants and water ice at cryogenic temperatures (Nurge 2012) show a significant increase of ε_r in the frequency range below 100 Hz. Lunar subsurface ice is stable over geologic timescales at temperatures around 110 K and can be found at shallow depths accessible by PROSPECT (Paige *et al* 2010, Schorghofer and Aharonson 2014, Hayne *et al* 2015, King *et al* 2020, Reiss *et al* 2021). An *in-situ* measurement of the dielectric constant versus frequency and temperature therefore allows to detect the presence of water ice in lunar regolith.

1.3. Permittivity sensor heritage and concept

In the terrestrial environment, and also in many planetary environments, the conductivity of materials of interest (solids, plasma, etc) is sufficiently high so that electrode to medium contact becomes a relevant error source for the measurement of the complex permittivity. A quadrupolar measurement is required to enable an accurate measurement under these conditions (Wenner 1916). This principle was applied in several examples of space instrumentation, including the Huygens Atmospheric Structure Instrument's (HASI) Mutual Impedance Probe (Ferri *et al* 2002) and the permittivity probe of the SESAME package on Philae (Seidensticker *et al* 2007). The lunar environment, on the other hand, is characterized by a high vacuum and regolith with extremely low DC/ELF conductivity in the range of $\sim 10^{-16}$ mhO m^{-1} (Carrier *et al* 1991), similar to good terrestrial isolators. This allows to assume an injected electrode current as almost purely capacitive and significantly reduces the electrode-medium interface issues present in the aforementioned environments. It allows to perform measurements with acceptable accuracy also with a single electrode measurement, as long as the contact of the electrode to the medium is characterized to a sufficient degree. An early prototype for a permittivity sensor integrated in a mole-type carrier (Trautner *et al* 2004) demonstrated the capability to measure the dielectric constant of isolating materials with a single electrode by monitoring the AC electrode current. The PROSPECT permittivity sensor is based on this concept, and uses a single electrode integrated in the ProSEED drill rod of the PROSPECT package (Trautner *et al* 2018).

2. Sensor description

2.1. Measurement principle

The sensor performs its function by measuring the AC current emitted from an electrode into the surrounding medium.

For the PROSPECT sensor, the detection of water ice at cryogenic temperatures is among the key objectives, therefore a frequency range from 1.5 Hz to ca. 100 Hz was chosen. Measurement frequencies are not applied in sequence (as it was done for the HASI and SESAME instruments) but applied concurrently, which allows to minimize the sensor complexity and associated mass, dimensions and power consumption.

A digital signal generator provides a square wave voltage signal of 1.5 Hz with 50% duty cycle. According to the Fourier theorem, this type of signal can be represented by

$$
\begin{aligned}
x(t) &= v\frac{4}{\pi}\sum_{k=1}^{\infty}\left(\frac{\sin\left(2\pi\left(2k-1\right)ft\right)}{2k-1}\right) \\
&= v\frac{4}{\pi}\left(\sin\left(\omega t\right) + \frac{1}{3}\sin\left(3\omega t\right) + \frac{1}{5}\sin\left(5\omega t\right) + \dots\right)
\end{aligned} \quad (3)
$$

where $\omega = 2\pi f$ and v is a magnitude scaling factor. With $f = 1.5$ Hz, this signal includes frequency components at 1.5 Hz, 3.0 Hz, 4.5 Hz etc. with magnitudes that are decreasing with $\frac{1}{(2k-1)}$.

When the voltage signal components $x_k(t)$ are applied to a capacitor with complex impedance

$$
Z_{C_k} = -j * X_{C_k} = \frac{-j}{\omega_k C_k} \quad (4)
$$

where

$$
\omega_k = (2k-1)2\pi f \quad (5)
$$

and

$$
C_{(2k-1)} = C_0 * \varepsilon_{(2k-1)} \quad (6)
$$

where C_0 is the capacitance in vacuum without dielectric, and $\varepsilon_{(2k-1)}$ is the dielectric constant of the capacitor's dielectric at frequency $f*(2k-1)$, the magnitude of the resulting capacitor current is described by

$$
\begin{aligned}
|i_C| = \frac{x(t)}{Z_C} &= 8vfC_0\left(\sin\left(\omega t\right)\varepsilon_1 + \sin\left(3\omega t\right)\varepsilon_3 \right. \\
&\left. + \sin\left(5\omega t\right)\varepsilon_5 + \dots\right).
\end{aligned} \quad (7)
$$

It therefore follows that the capacitor current magnitude is constant for all included frequencies, if the capacitance is constant over the frequency range of interest, as is the case for vacuum. If the capacitor is filled with a medium of ε_k that varies with frequency, this will lead to a variation of the currents over frequency, and a measurement of the currents will allow to determine the dielectric constant vs. frequency of the medium in the capacitor. A sequence of discrete samples allows to derive a dielectric spectrum via Fourier analysis.

2.2. Mechanical design and accommodation

The permittivity sensor consists of two main hardware elements, an electrode carrier assembly (ECA) and a printed circuit board carrier assembly (PCA). The ECA is accommodated in the front part of the ProSEED drill rod, about 40 cm
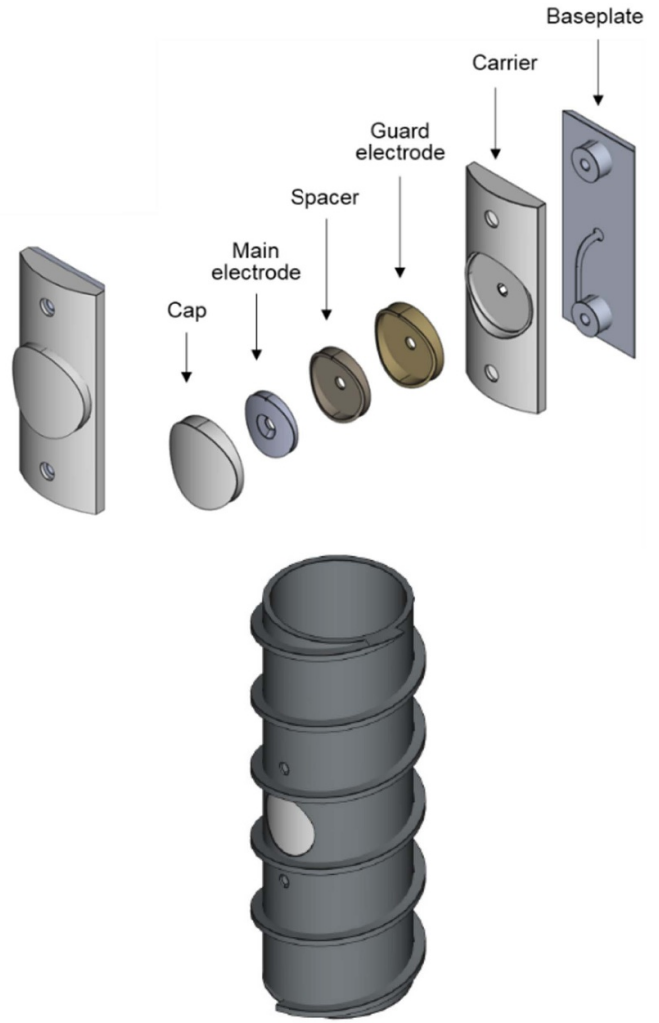
Figure 1. Permittivity sensor electrode elements and integration in ProSEED drill rod.

from the drill tip, right above the sampling mechanisms that occupy the drill's front section. The ECA includes sensing electrode, guard electrode, structural and mounting elements, and the coaxial cable that connects the ECA to the PCA, which accommodates the electronics.

The PCA consists of the printed circuit board and of structural elements that allow installation in the upper end of the drill rod. The PCA shape ensures an adequate distance of the electronics from the drill-integrated harness in order to minimize noise and crosstalk levels.

The complex geometries of ECA and PCA will be realized by additive manufacturing using polyether-ether-ketone (PEEK) for isolating parts and conductive PEEK for the electrodes. Only the back plate of the ECA will be machined from aluminium. Figures 1 and 2 illustrate the ECA and PCA design.

2.3. Electronics architecture

In the PROSPECT permittivity sensor, a square wave signal is generated using a digital oscillator. This signal is filtered
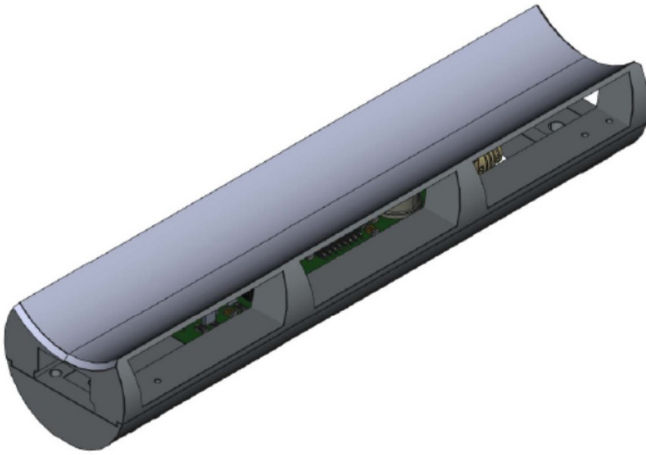
Figure 2. Permittivity sensor electronics embedded in mounting structure for ProSEED drill rod integration.

using a first order 50 Hz low pass in order to limit the resulting peak magnitude of the cumulative capacitor current in the time domain. The resulting signal is then applied to the sensing electrode via a current measurement resistor R_M. The low pass output is also used for the guard signal that reduces parasitic capacitance on the printed circuit board, in the harness, and in the electrode carrier structure. The electrode current is measured via the voltage across the resistor R_M. This voltage is then amplified and made available at the sensor output. It is conditioned and sampled via an analogue input of the ProSEED electronics unit (Trautner *et al* 2018) and stored in a dedicated data structure as part of the ProSEED data pool. A block diagram illustrating the PROSPECT sensor design is shown in figure 3. The sensor output signal in time and frequency domain are shown in figure 4.

The sensor electrode emits a small AC current of few pA through an isolating electrode cap that protects the electrode from electrostatic effects and mechanical stress during drilling. The emitted current crosses the gap between cap surface and borehole wall and penetrates the subsurface regolith. The electric circuit is closed via the drill rod and lander chassis. Parasitic capacitances C_{P1} (in electronics) and C_{P2} (in electrode), as well as the capacitance of the electrode cap C_{E-CAP} are constant and are measured as part of the sensor calibration. The gap dimension depends on borehole characteristics, and the fill state of the auger flutes of the drill. The auger gap can be emptied by rotating the drill without forward thrust, or can be filled to a high degree by using a high drilling speed. The optimal modes for permittivity sensor measurement will be tested during the ProSEED drill test and qualification campaigns.

The sensor electronics design utilizes only three active semiconductor components with small pin numbers and package footprints, which simplifies space qualification for an extended temperature range. Key characteristics of the sensor are summarized in table 1. The geometry of the electric field that governs the emission of the electrode current is shown in figure 5.

2.4. Sensor operations concept

The operation of the permittivity sensor includes calibration measurements in vacuum as well as measurements performed when the sensor's electrode is at or below lunar surface level.

For calibration, the drill deployment is stopped in a position where the electrode is exposed to vacuum and no spacecraft structures or lunar materials are close to the electrode. The signals measured in this position constitute the reference for a dielectric constant of 1. The drill deployment is then resumed and subsurface measurements are performed at certain depth intervals during the drilling process. For these subsurface measurements the drilling process is interrupted. The filling fraction of the auger gap with drill cuttings can to some extent be controlled via different drill rotation modes by applying different speeds and vertical thrust. The cuttings cone that builds up at the surface is monitored by the ProSEED imaging system as part of the PROSPECT operations (Trautner *et al* 2018), allowing an estimate of the volume and density of excavated soil. For measurements in soil, the permittivity sensor can take either single point measurements or an azimuth scan along the drill rod rotation.

Single point measurements are performed at a specific depth and single drill rod azimuth direction. This is envisaged to be employed predominantly for ice detection, where measurements are taken over an extended timeframe to allow averaging of multiple measurement results and for exploiting the temperature dependence of the ice/regolith mix.

For the azimuth scan, the drill is moving through a full rotation in steps of 45° (8 positions), 22.5° (16 positions) or 15° (24 positions). Measurements taken at these azimuth positions allow to construct a three-dimensional map along depth, corresponding to an electrical image that provides information on borehole shape, average dielectric constant and inhomogeneous inclusions such as rocks. The number of steps in azimuth and depth depend on operational constraints such as available time and energy.

For the detection of subsurface ice, the sensor can be used in two different operation modes described in the following. Ice detection via both modes will be enhanced to provide quantitative results and constraints by employing models for the soil temperature and the electrode to soil interface.

2.4.1. Ice detection in time/temperature mode. Here, the temperature dependency of the dielectric constant in ice-bearing regolith is exploited. The drill is stopped and measurements are taken at periodic intervals. Between measurements, the drill rod heaters are activated in order to progressively warm up the drill rod and the adjacent regolith. The change of the signal in the frequency domain is analyzed, revealing the presence of ice in the form of an increasing signal mainly at the low frequency end of the spectrum.

2.4.2. Ice detection in reference subtraction mode. In this mode, measurements are taken only during a short time interval, typically a few seconds. For the analysis in the frequency domain, calibration measurements taken in vacuum or in dry
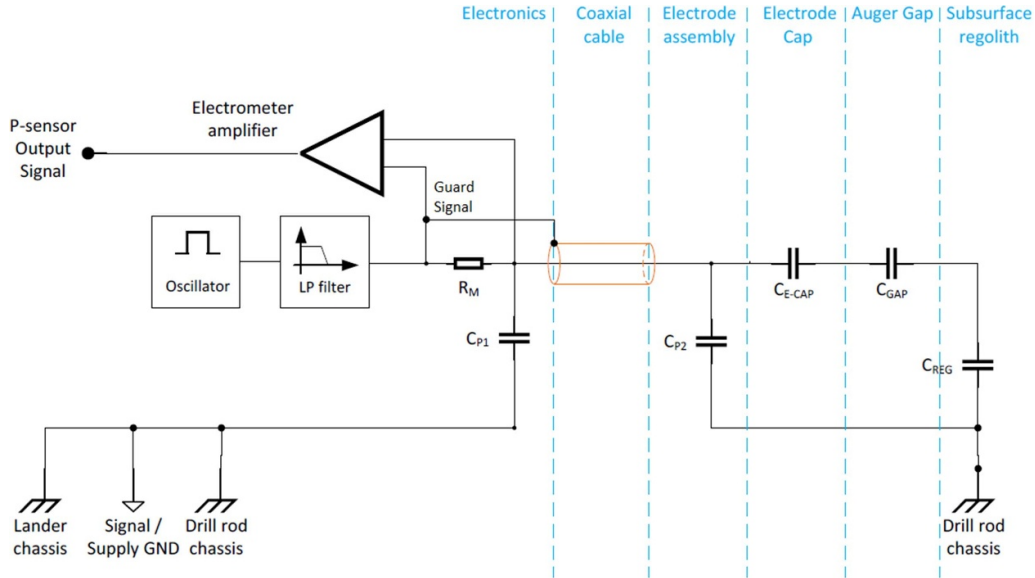
Figure 3. Permittivity sensor block diagram and path for emitted signal from electrode via regolith.

regolith (where the dielectric spectral response is flat) are taken as a reference baseline. The reference measurement is scaled up to match the magnitude of the measured spectrum in a band that is not enhanced by the presence of ice at the soil temperature and the scaled reference spectrum is subtracted from the measured spectrum. The presence of ice will be detected by an enhancement of the signal at the low frequency end of the spectrum.

3. Error sources and sensitivity

The measured capacitance C_m is a sum of parasitic capacitance C_{para} and electrode capacitance C_{el}:

$$C_m = C_{el} + C_{para}. \tag{8}$$

The parasitic capacitances in the electronics, harness and electrode assembly are constant, and their measurement is included in the calibration versus temperature and voltage. They are subtracted from the measured capacitance in order to obtain the electrode capacitance. Error contributions related to supply voltage and electronics temperature have been evaluated on the sensor prototype. On PROSPECT, both the supply and temperature will be monitored in housekeeping data with accuracies better than 0.3% and ∼2 K, respectively. The resulting measurement error related to supply voltage is negligible, as the sensor will be calibrated periodically in vacuum outside the borehole. The expected temperature-related error is <0.1%. Both errors apply uniformly to all spectral signal components.

The electrode capacitance can be coarsely approximated by a series circuit of electrode cap capacitance C_{cap}, auger gap capacitance C_{gap}, and capacitance in the regolith C_{reg} (see also figure 3):

$$C_{el} = C_m - C_{para} \approx \frac{1}{\frac{1}{C_{cap}} + \frac{1}{C_{gap}} + \frac{1}{C_{reg}}}. \tag{9}$$

While the cap capacitance is constant, the capacitance of gap and regolith are variable. The latter is directly affected by the regolith dielectric constant. The gap capacitance is affected by the fill fraction of the soil cuttings in the auger gap and their density (figure 6). Accurate results for the regolith dielectric constant will be obtained by matching measurement data with results from finite element models of the configuration. The density of the soil cuttings in the auger gap are derived from images of the cuttings pile on the surface as they provide the ratio of excavated material volume to drill hole volume. The electrical properties of the soil cuttings can then be derived from models of electrical properties of granular materials, using relations such as the complex refractive index equation and others (Nelson 2004).

The auger fill state can be inferred from the drill speed and observed material transport (the cuttings pile formation on the surface is monitored by a camera). The auger gap can be cleared by stopping the drill forward motion while continuing the rotation which leads to continued transport of cuttings to the surface until the auger gap is nearly empty. The width of the auger-wall gap is variable within boundaries that can be constrained from drill experiments in a range of representative materials. These will be performed as part of the ProSEED drill qualification campaign.

A sensitivity analysis was performed to illustrate the change of the measured capacitance with auger gap and its fill state by using a COMSOL simulation model of the sensor electrode and the drill rod. For the undisturbed soil with a bulk density of 1.71 g cm^{-3}, a relative permittivity of $\varepsilon_{regolith} = 3$ was used. A value of $\varepsilon_{cuttings} = 2.3$ was assumed for the soil cuttings with a bulk density of 1.3 g cm^{-3}. These values correspond to a measurement depth of 35 cm, according to (1). Results are presented in figures 7 and 8. Due to relatively high
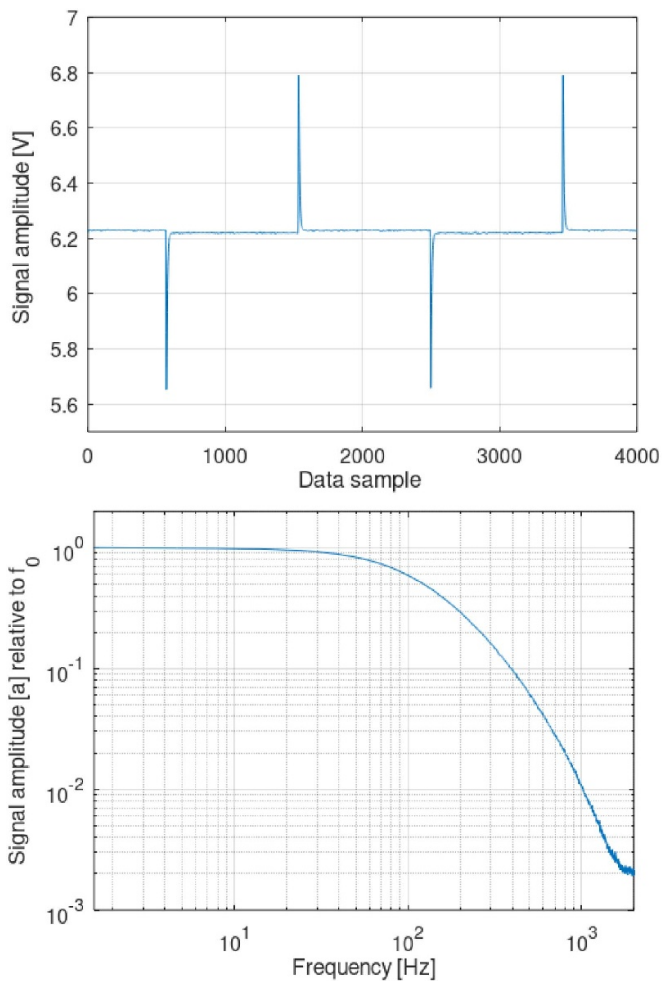
Figure 4. Permittivity sensor signal for electrode in air in time domain (top) and frequency domain (bottom).

Table 1. Key parameters of the PROSPECT permittivity sensor.

Parameter	Prototype	Flight model
Electronics PCB mass	7.8 g	Similar
Electronics PCB carrier mass	16.0 g	Similar
Electrode assembly mass	10.1 g	Similar
Total sensor mass incl. mounting materials	35 g	ca. 50 g
Electronics PCB size	$15 \times 70 \times 8$ mm	Similar
Electronics PCB carrier size	$\varnothing 22.6 \times 120$ mm	$\varnothing 29.5 \times \sim 120$ mm
Electrode assembly size	$36 \times 16 \times 6$ mm	$40 \times 16 \times 5$ mm
Electrode protrusion diameter	13 mm	15 mm
Active electrode area	60.8 mm^2	91.6 mm^2
Electrode cap thickness	<1.7 mm	0.5 mm
Supply voltage	12 V	12 V
Supply current, typ.	18 mA	<30 mA
Pulse frequency	1.5 Hz	1.5 Hz
Bandwidth	200 Hz 1st order	200 Hz second order
Sensitivity: max. electrode capacitance change for $\varepsilon_{\text{regolith}} = 3$ to $\varepsilon_{\text{regolith}} = 4$	0.072 pF	0.180 pF
Sampling rate	3 kSps	2 kSpS

nominal width of the auger gap of 2.9 mm, resulting from an auger flute width of 2.5 mm and an additional 0.4 mm gap to the borehole wall, the measurement is very sensitive to the auger fill fraction F. At $F = 0.5$, a 10% error in the estimation of the fill fraction results in a 18% error for the measured regolith permittivity $\varepsilon_{\text{regolith}}$. At $F > 0.8$ the error is reduced, but the related risk for the drilling activity due to possible clogging will allow reaching this state only under exceptional circumstances. At low $F < 0.15$ on the other hand, the electrode is not covered by regolith in the auger gap at all, and the error becomes negligible for an empty auger gap.

The measured capacitance also depends on the width of the gap between electrode cap surface and regolith of the borehole wall. While the nominal with is defined by the drill design, it may vary along the borehole and with electrode azimuth as a result of the drill's mechanical interaction with the subsurface material. Figure 8 shows the sensitivity of measured capacitance for variations of the auger gap width.

The minimum gap width is constrained by the auger width to 2.5 mm and may be reached at certain combinations of drill depth and azimuth in case of a deflection of the drill axis from the thrust axis. The maximum gap width depends on the stability of the borehole walls, but is constrained by the fact that the transport of drill cuttings requires friction between cuttings in the auger gap and the borehole wall. Tests of the drill in representative materials performed as part of the ESA PROSPECT project have typically resulted in smooth borehole walls with a limited number of spots of surface instability where the gap is widened.

Figure 8 shows model results that reflect the expected range of gap width for an empty gap and $\varepsilon_{\text{regolith}} = 3$. For a gap width variation of ± 0.4 mm with respect to the nominal value of 0.4 mm (defined by the difference in diameter of the cutting edge and auger), the measured electrode capacitance varies by -3.0% to $+4.2\%$. Without additional correction, this corresponds to an error of -23% to $+27\%$ for $\varepsilon_{\text{regolith}}$, as obtained from a data fit to COMSOL model results for nominal gap width.

The nominal measurement mode for permittivity measurements is an azimuth scan with 8 or 16 measurements. In case of a non-symmetric position of the drill rod in the borehole (for example as a result of forces on the drill bit resulting from buried angled hard rock surfaces), the measured capacitance versus azimuth provides information on the asymmetry, which can be used for additional corrections. The resulting signal versus azimuth is shown in figure 9 for an axis misalignment of 0.4 mm. Also shown is a (conservative) relative measurement error from prototype sensor laboratory tests of 0.23%.
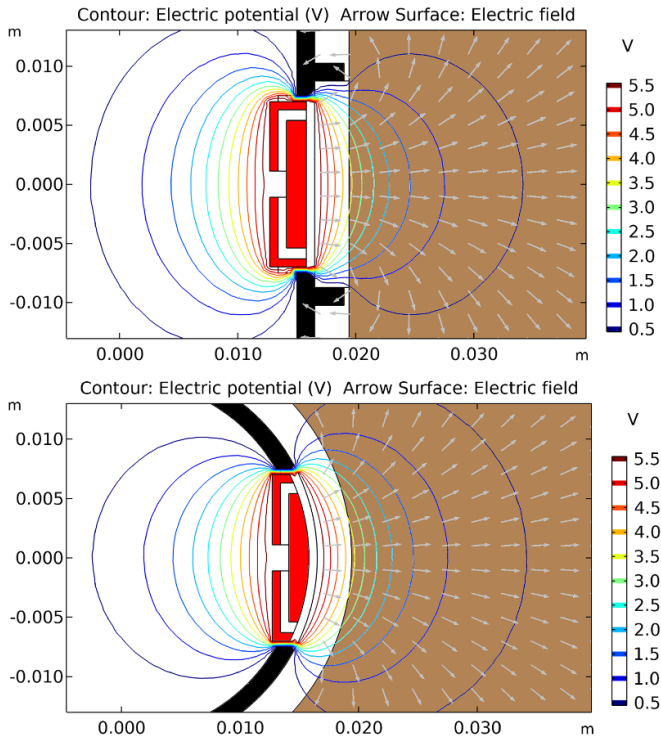
Figure 5. Electrode electrical field geometry as seen in vertical (top) and horizontal (bottom) drill rod cross-sections. The signal and guard electrodes (red) are integrated in the drill rod (black). The measured electrode current (depicted via grey arrows) flows through the regolith (brown) while passing through the isolating electrode cap and the auger gap (empty in this figure, empty or partially filled with regolith during ProSEED operation).
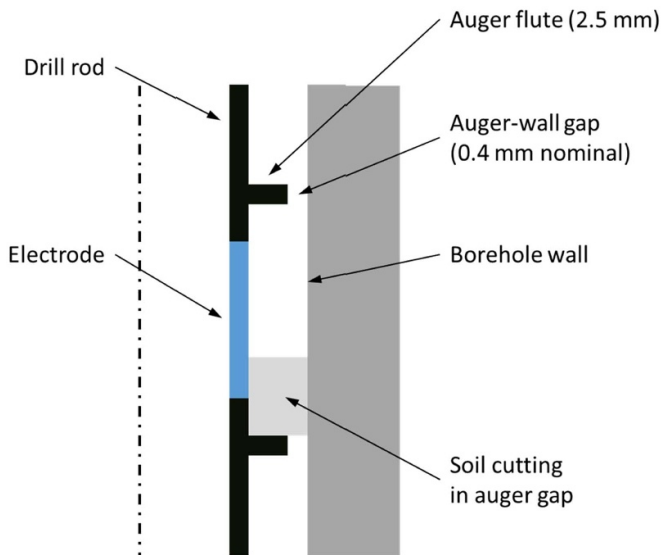

Figure 6. Geometry of drill rod, electrode, auger-wall gap, and soil cuttings in electrode to borehole wall gap.

The signal deviation versus azimuth is ∼8 times larger than the standard deviation for a single measurement, and a fit of 16 or more data points will therefore allow to estimate the axis misalignment with an error of <0.02 mm.
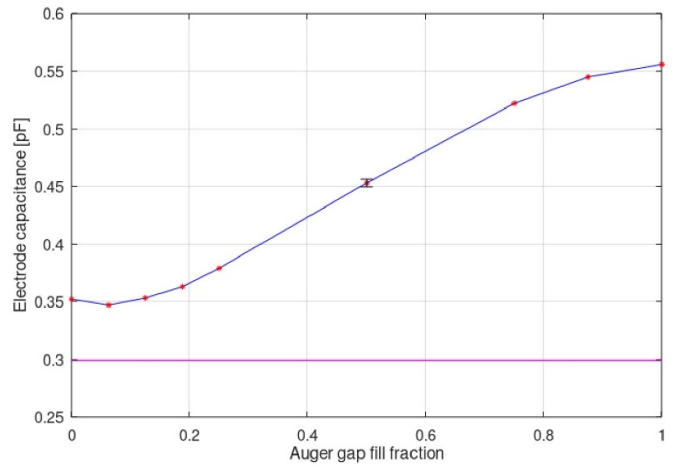

Figure 7. Simulated electrode capacitance vs. auger gap fill fraction (linear, vertical) for $\varepsilon_{\text{regolith}} = 3$ and $\varepsilon_{\text{cuttings}} = 2.3$ (blue line) for the flight model design. The capacitance for the electrode in vacuum is plotted for comparison (magenta line). The error bar at fill ratio 0.5 illustrates the prototype sensor standard deviation of 0.23% for a 3 s measurement.
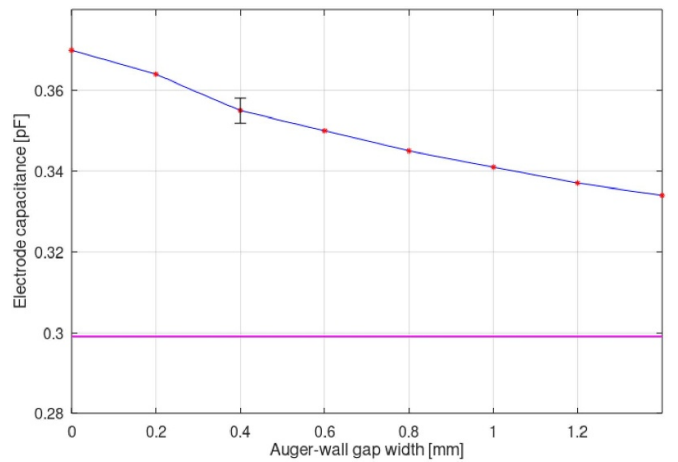
Figure 8. Simulated flight design electrode capacitance vs. auger-wall gap width for $\varepsilon_{\text{regolith}} = 3$ (blue line). The capacitance for electrode in vacuum is plotted for comparison (magenta line). The error bar at the nominal auger-wall gap width 0.4 mm illustrates the prototype sensor error for a 3 s measurement.

Using a model of the drill/borehole axis misalignment and data fits with numerical models, the gap width for each individual measurement can be reconstructed and used for data calibration, resulting in an error for $\varepsilon_{\text{regolith}}$ that is dominated by the error in the modelled borehole diameter. This parameter is initially defined by the drill bit diameter and then increases with borehole wear, which is a function of subsurface material as well as drilling speed and drilling duration. Increasing wear widens the borehole and reduces the measured capacitance. For a borehole diameter error of ± 0.4 mm (averaged over borehole surface patches of a size similar to the electrode area), the expected relative error for $\varepsilon_{\text{regolith}}$ is $-12/+13\%$. Further accuracy improvements will be possible by using data from
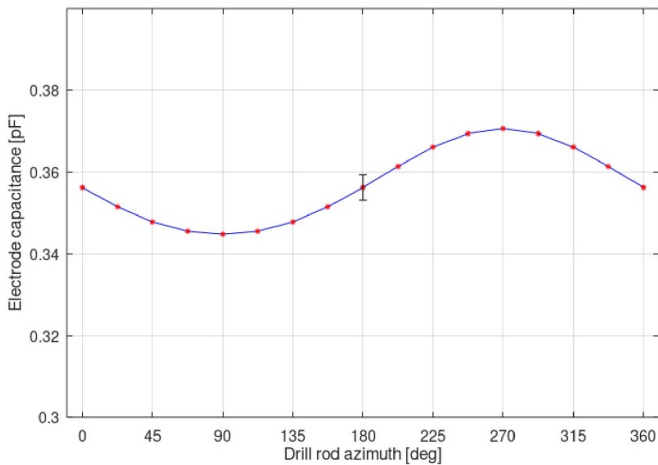
Figure 9. Simulation of measured capacitance for a borehole diameter of 38.8 mm with borehole/drill vertical axis misalignment of 0.4 mm. The error bar at 180° azimuth illustrates the (conservative) relative measurement error of 0.23% for a standard duration time domain measurement.

multiple azimuth scans and a higher number of data points per scan.

4. Comparison and novelty of the sensor concept

A comparison with previously flown sensors or instruments for permittivity measurements is provided in table 2. Quadrupolar probes (Ferri *et al* 2002, Seidensticker *et al* 2007) developed for meter-scale atmospheric and surface measurements provide good accuracy (10% and better), thanks to the principle of using four or more electrodes for the measurement. Their electrodes are accommodated on lander structures (booms, landing gear), which complicates a mass comparison with simpler designs. Nevertheless, a mass reduction factor of around 10–20 for less complex designs that measure on centimeter scale, like TECP (Zent *et al* 2009) and the PROSPECT permittivity sensor, is evident. Both simpler designs can be expected to provide a lower accuracy due to the uncertainties in the electrode to soil coupling impedance. The high measurement frequency of TECP (8 MHz) improves this situation to some degree. However, the relatively high conductivity of Martian soil, as compared to lunar regolith, in a warmer Martian environment aggravates the problem for absolute permittivity measurements. Only relative TECP measurement results have been published so far (Zent *et al* 2010). Our sensor uses only one small electrode (the signal return being via drill and spacecraft chassis with much better coupling to the regolith). The electrode/regolith geometry is reasonably well constrained, and the sensor measures in lunar regolith with typical conductivity of $\sim 10^{-14}$ mho m^{-1}, which is several orders of magnitude lower than that expected for Martian soil. The capability of our sensor for absolute permittivity measurements in the lunar environment has been assessed in section 3. Its power consumption is approximately factor 10 lower than that of the Huygens design, and comparable to the SESAME PP consumption, both of which utilize data acquisition and

processing by a shared processing unit to minimize resource consumption.

The PROSPECT permittivity sensor is the first to be integrated in a planetary drill. It is also the first permittivity sensor to replace sinusoidal signal generation via ADC followed by on-board digital signal processing (as compared to FFT in HASI-PWA, wavelet processing in SESAME-PP), with lossless onboard data compression of the sensor data and transmission of the compressed time domain signal for FFT processing on ground. This allows to acquire the dielectric spectrum with a single square wave excitation frequency, and enables a drastic simplification of the flight hardware. The sensor is expected to provide the first *in-situ* measurement of the dielectric constant of subsurface regolith on the Moon.

5. Laboratory tests

A stationary prototype of the permittivity sensor has been tested in ambient and cryogenic conditions in order to confirm the capability for ice detection. The tests employed a flight-like electronics board and an electrode with representative overall design, but with smaller dimension compared to the flight design (13 mm instead of 15 mm outer diameter), and a thicker electrode cap (maximum thickness of 1.6 mm instead of 0.5 mm). The electrode was mounted in a stainless-steel tube of 30 mm diameter supplementing the drill rod. The sensor was first tested and calibrated in air, and then immersed in a mixture of glass beads and water, cooled using liquid nitrogen (LN2). Glass beads were chosen as a regolith simulant due to their representative electrical properties, as the dielectric constant of dry beads is similar to lunar regolith, showing a flat frequency response in dry condition at room temperature and also at very low temperature in mixture with water. Also, the glass beads have a well-defined particle size, which was beneficial for avoiding electrode contamination by small particles. The tests were performed in a laboratory environment with a computer-based data acquisition system. The test setup is shown in figure 10.

There was no air gap between electrode cap and glass beads. Electromagnetic interference (EMI) from noise sources such as laboratory equipment and lighting was reduced as far as possible via twisted pair signal wires and shielding. The electrode/steel rod assembly was immersed into the precooled glass beads/water mixture ($\sim$9% water by mass), which included two temperature sensors at a few centimeters distance from the electrode. Before the start of the measurement, additional LN2 was added to the mixture to freeze the water and ensure a low temperature starting point below 80 K. Measurements were taken at frequent intervals over a 12 h timeframe, during which the setup was not altered. The measured temperatures were corrected using results from a COMSOL thermal model to obtain the temperature at the electrode location, with a resulting error estimated <6 K.

The sensor data was analyzed in frequency domain using both proposed data analysis methods for ice detection. Figure 11 shows the spectra of measurements taken at sample

Table 2. Comparison of permittivity instruments and sensors for space applications.

|	HASI-PWA	SESAME-PP	TECP	PROSPECT P-sensor
Mission	Huygens (Titan)	Philae (Comet 67P)	Phoenix (Mars)	Luna-27 (Moon)
Type	Quadrupole array technique	Quadrupole array technique	Double rod capacitance sensor	Single electrode capacitance sensor
Medium	Atmosphere	Cometary surface	Martian soil	Lunar regolith
Accommodation	Platform & deployable booms	Platform, landing gear, P/L elements	Robotic arm	Drill rod
Frequency	45 Hz to 6 kHz, sine wave	10 Hz to 20 kHz, sine wave	8 MHz, square wave	1.5–200 Hz, square wave
Measurement accuracy	Demonstrated better than $\pm 10\%$	Achieved $\pm 8\%$ (stated for mission results)	No accuracy information published	Ca. $+12/-13\%$ expected (see section 3)
Electrode configuration	2 booms, each with 1 TX and 1 RX electrode	1 TX + 2 RX in landing gear; 2 RX on APX + MUPUS	2 needle electrodes	1 electrode + chassis
Hardware size	Booms 505 mm long; ring electrodes Ø65/Ø100 mm; PCB 158.9 × 162.0 mm	Foot electrodes Ø101 mm each; APX/Pen similar; PCB 120 × 100 mm	Overall dimensions 16.64 × 40.64 × 118.76 mm^3; 15 mm long electrode rods	ECA 36 × 16 × 6 mm; Electrode Ø10.8 mm; PCA Ø22.6 × 120 mm
Instrument/Sensor mass	PCB mass 725 g (PWA + preamplifiers)	Electrodes & preamplifiers <170 g; electronics 270 g	Estimated ~40 g	Estimated ~50 g
Power consumption	~3.5 W (incl. processing H/W)	≤320 mW (w/o processing H/W)	No separate information published (part of MECA)	<360 mW (w/o processing H/W)
References	Falkner (1999), Ferri et al (2002), Fulchignoni et al (2002), Trautner et al (2003).	Moehlmann et al (1998), Seidensticker et al (2007), Lethuillier et al (2016), DLR (2021).	Zent et al (2009), Zent et al (2010)	This paper
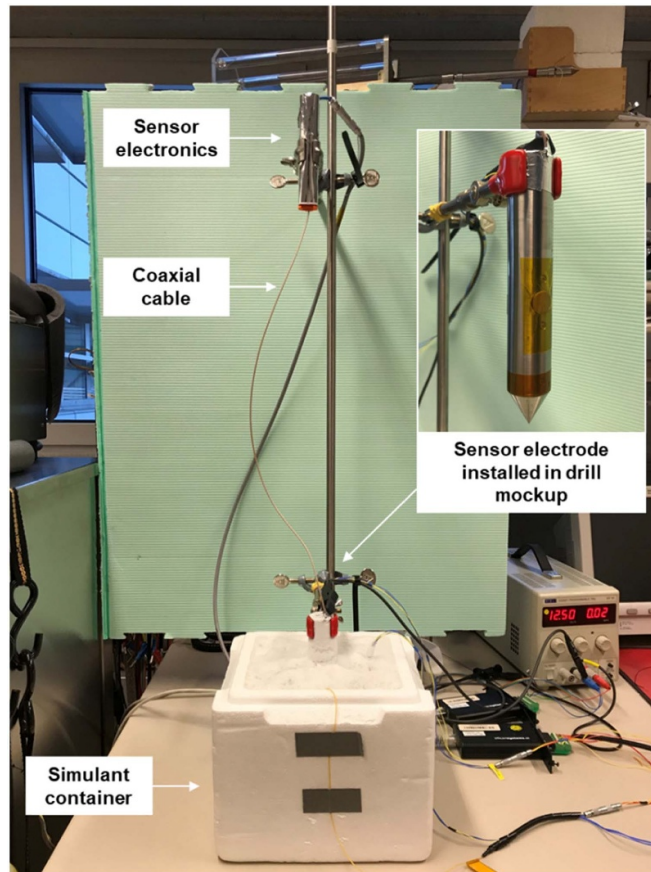
Figure 10. Laboratory setup for testing the permittivity sensor with regolith simulant in cryogenic conditions.
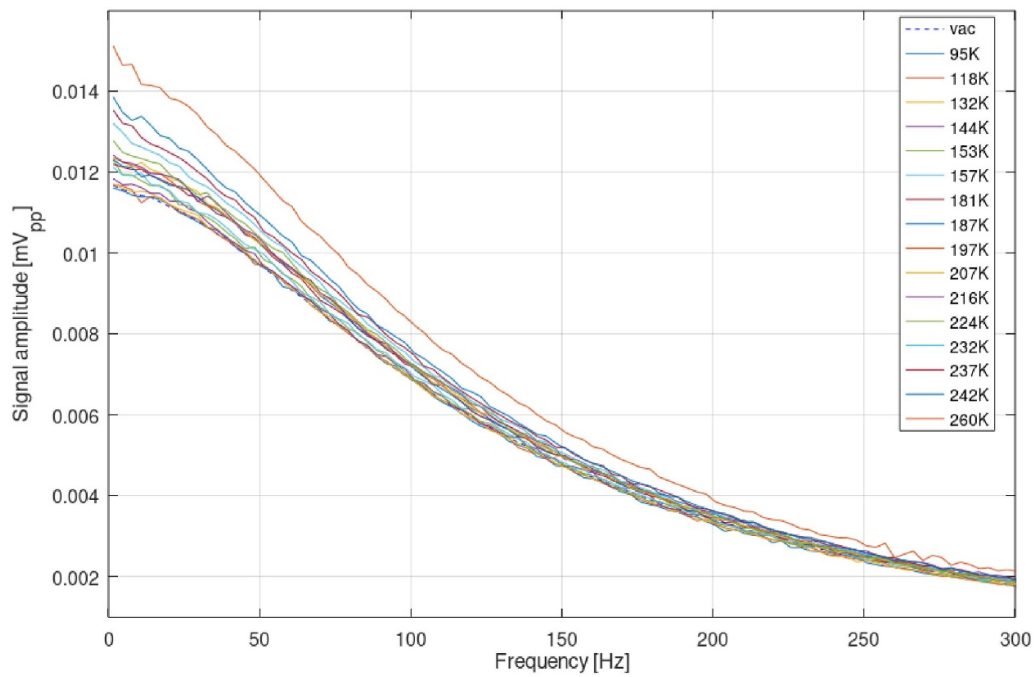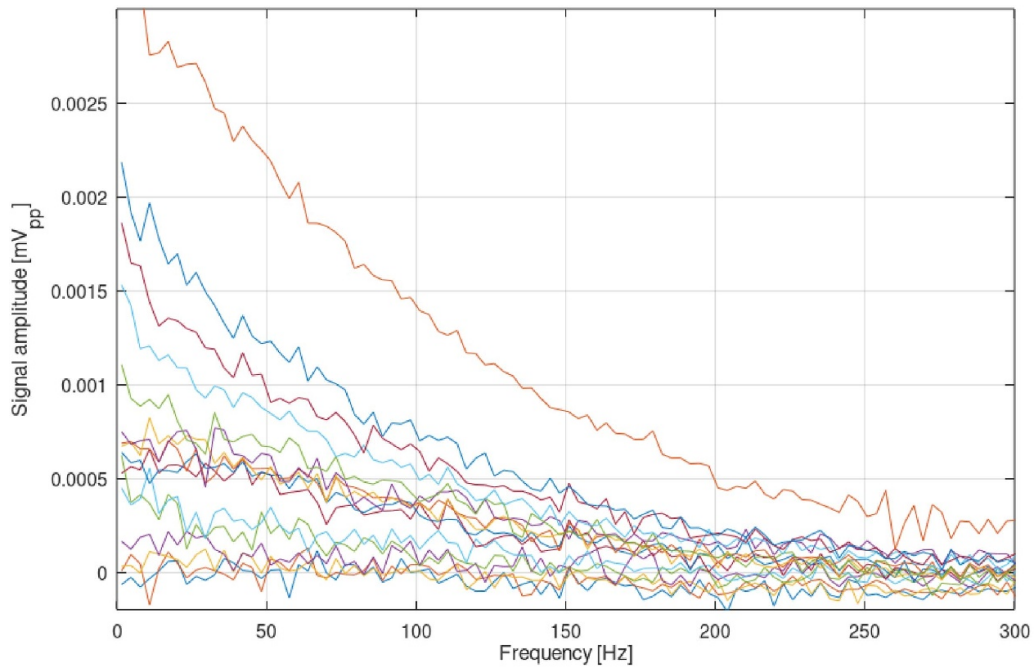

Figure 11. Sensor signal spectra acquired during cryogenic tests of a prototype permittivity sensor with flight-like electronics and electrode immersed in water ice bearing simulant.

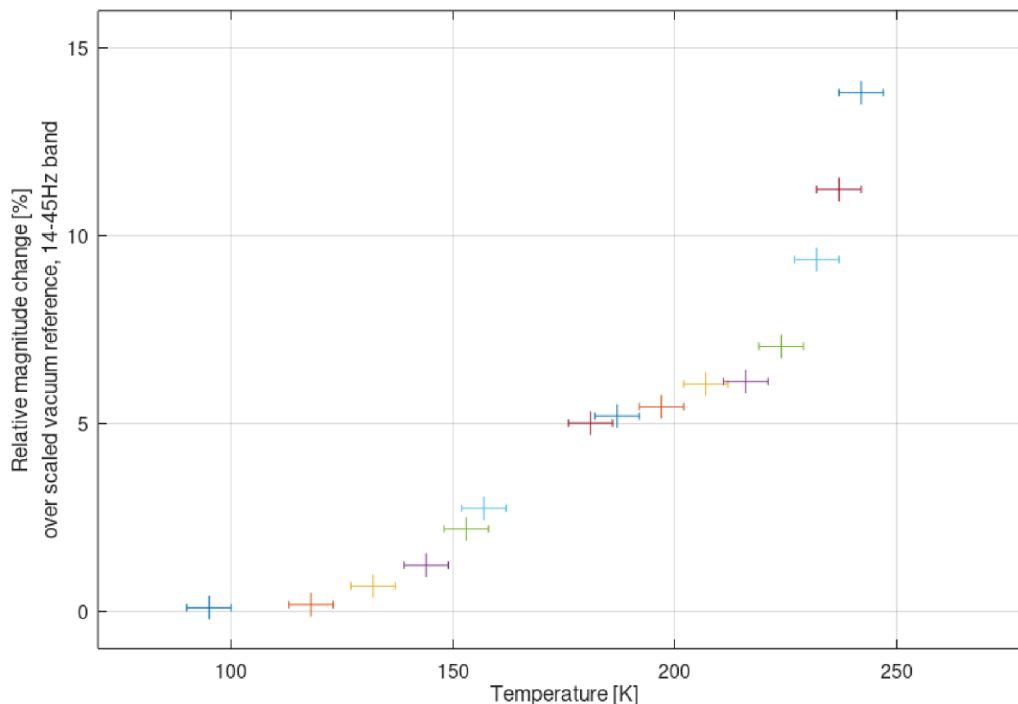**Figure 12.** Sensor signal spectra acquired during cryogenic test of prototype permittivity sensor with flight-like electronics and electrode immersed in water ice bearing simulant, after subtraction of scaled vacuum signal. The legend (color coding of individual curves) equals the one displayed in figure 11.

Figure 13. Relative magnitude change of the prototype permittivity sensor signal in the 14–45 Hz frequency band from test in water ice bearing simulant.

temperatures of 78 K up to 242 K. It includes the effects of the 50 Hz low pass filter (see figure 3) and the ∼1 pF parasitic capacitance in the sensor electronics, which are both constant. The trend in increasing electrode currents and the enhancement in low frequencies is clearly visible and represents the time/temperature detection method described in section 2.4.

Figure 11 also includes a scaled vacuum reference (dashed line) obtained via scaling the vacuum signal taken at room temperature to match the 95 K signal level in the 55–85 Hz band, which was selected due to the low EMI level.

Figure 12 shows the difference of measured spectra and scaled vacuum reference, illustrating the reference subtraction

detection method. The signal increase over temperature, especially below 200 Hz, is clearly visible, providing evidence for the presence of water ice in the simulant.

For additional noise suppression, the signal is averaged for each measurement in a frequency band with pronounced water ice signature and at comparatively low noise level. The result for the band of 14–45 Hz is plotted over temperature in figure 13, with error bars corresponding to the thermal model error and the observed standard deviation (0.3%) for the capacitance measurement in the selected band.

The data suggests that, for the employed measurement configuration and procedure (prototype electrode design, laboratory environment, measurement duration of 3 s per temperature point), the detection temperature limit for ∼9% by mass water ice is near ∼125 K, where a small signal increase is notable. A more prominent 3% signal increase is observed near 160 K. As a first approximation, the relative signal increase over temperature is proportional to the ice content in the simulant. Therefore, for a water ice mass fraction of ∼1% representative for a lunar scenario, we conservatively estimate the detection temperature limit to be lower than 160 K. It is noted that these values are derived from the permittivity sensor prototype with a non-optimized design and in the described laboratory setup, with the main error source being EMI noise from the laboratory environment. This noise level from external sources can be further reduced by increasing the measurement duration and averaging of multiple measurements.

6. Summary of sensor performance

The analysis of the FM electrode performance demonstrates that the highest accuracy for measuring $\varepsilon_{\text{regolith}}$ is achievable via azimuth scans with emptied auger gap, which is the operational baseline. For the detection of water ice, the highest sensitivity is achieved when a high fill ratio of the auger gap is established via high vertical drill speed before performing a series of measurements. In this operational mode, the achievable accuracy depends predominantly on the accuracy of estimating the auger fill fraction. The shape of the borehole and its alignment with the drill axis can be estimated from the permittivity measurements in an azimuth scan and are useful supplementary data to support the analysis of the drilling process.

The permittivity sensor prototype has demonstrated its capability for ice detection at cryogenic temperatures for short measurements of 3 s and in a laboratory environment. For PROSPECT, single measurement durations up to 32 s can be programmed, and an arbitrary number of measurements in a stationary drill configuration can be performed in sequence, which allows further noise reduction. The noise level for the flight configuration depends on the properties of various PROSPECT elements and cannot yet be predicted. It is however expected to be much lower compared to the laboratory environment. Further sensitivity improvements have already been implemented for the FM design of the permittivity sensor, such as a larger electrode diameter, thinner electrode cap, and a more efficient guard design (see table 1).

The increase in sensitivity of factor 2.5 by design, in combination with increased measurement duration and data averaging without laboratory noise related frequency band restrictions, is expected to allow detection of an ice mass fraction of 1% at temperatures down to 125 K and possibly below. The sensitivity for ice detection can further be increased by heating the ProSEED drill rod and the adjacent regolith using the drill internal heaters. The sensor is therefore capable of detecting and constraining the quantities of ice expected in lunar polar areas based on existing data (e.g. Colaprete *et al* 2010). It also allows to distinguish between subsurface regolith ($\varepsilon_{\text{regolith}} \approx 3$) and embedded rocks ($\varepsilon_{\text{rock}} \geq 4$) with a typical relative signal change of 4% up to >25% depending on the auger filling.

A detailed characterization of the relationships of drill operation modes, gap fill fraction, gap width, and borehole shape will be part of the ProSEED QM/FM test campaign. This will also include an updated evaluation of the FM permittivity sensor performance for ice detection.

7. Future sensor applications

The permittivity sensor concept chosen for the PROSPECT implementation is driven by the accommodation constraints of the ProSEED drill rod, which puts severe restrictions on electrode design and placement. However, future lunar missions to prospect for surface and subsurface ice with landers and rovers will provide less severe design constraints. While the sensor electronics presented here can easily be re-used or integrated with other electronics on a shared electronics board, the electrode configuration can be modified for an alternative accommodation, for instance integrated in landing gear, placed on a rover hardware element that can be lowered to the surface, or integrated in a vehicle wheel. Figure 14 illustrates two options that allow sensing the regolith to a depth that is approximately proportional to the electrode diameter. An integration on the foot of a lander or hopper will allow measurements of surface/subsurface electrical properties at the landing sites. An electrode accommodated on a rover wheel will allow periodic measurements along the rover track. Both configurations imply a much larger electrode in comparison to the PROSPECT sensor electrode. Furthermore, the electrodes are put in close contact with the regolith by nature of the accommodation, providing a much improved sensitivity and measurement accuracy.

8. Conclusions

The detection and characterization of lunar resources, including water ice, is a key area of interest for a new generation of lunar missions. Ice exhibits a distinct signature of the dielectric constant in the ELF range even at cryogenic temperatures. The PROSPECT package developed for flight on Luna-27 will include a novel permittivity sensor as part of the ProSEED drill. The sensor hardware mass is ∼50 g and is based on simple and lightweight electronics. It supports subsurface measurements of the dielectric constant in a bandwidth
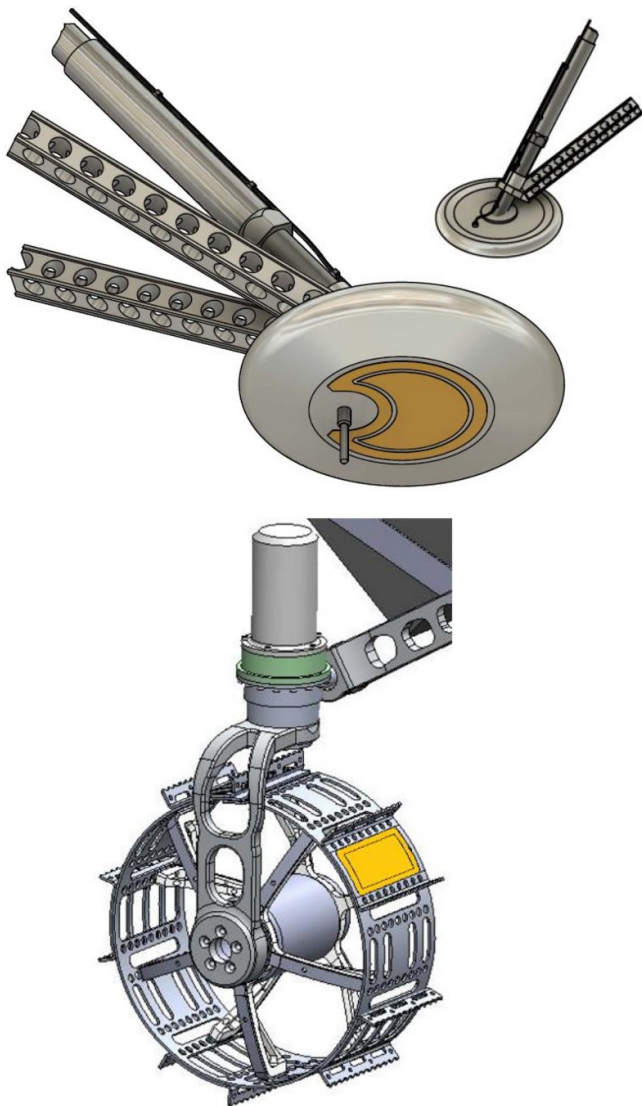
Figure 14. Permittivity sensor electrode accommodation options for future lunar missions. Top: accommodation on landing gear footpad; Bottom: accommodation on rover wheel. A single coaxial cable is required to connect electrode/guard ring (yellow areas) and electronics.

of 1.5–200 Hz. Finite element models of the configuration of electrode and subsurface regolith support the data analysis and the optimization of operational strategies. The control and characterization of the electrode-regolith interface is important for achieving the desired measurement accuracy and can be established via identified operational means and suitable measurement approaches.

As shown by simulations, the expected relative error for measurements of $\varepsilon_{\mathrm{regolith}}$ is on the order of 10%−15%. The main error contribution stems from uncertainties in the borehole shape and its alignment with the drill axis, which affects the gap size between electrode and soil. The sensor data supports a characterization of the borehole shape and its alignment with the drill axis, which are useful additional data that support the analysis of the drilling process.

The sensitivity of the sensor for detection of water ice at cryogenic temperatures is sufficient to detect ice at

concentrations relevant for future resource prospecting and towards *in-situ* resource utilization. The prototype sensor demonstrated detection of ∼9% water ice at 125 K based on 3 s measurements. The larger flight model sensor is expected to allow detection of 1% ice at that temperature with increased measurement duration. The sensitivity for ice detection can be further increased by locally warming up the regolith using heaters integrated in the ProSEED drill. Due to its low mass, low power, simplicity and short measurement time, the permittivity sensor concept is suitable to detect lunar water ice on many types of deployment platforms. Alternative configurations for future missions include electrodes integrated in rover wheels or landing gear footpads.

Data availability statement

The data that support the findings of this study are available upon reasonable request from the authors.

Acknowledgments

ORCID iDs

R Trautner ⓘ https://orcid.org/0000-0002-5190-2894
P Reiss ⓘ https://orcid.org/0000-0002-5199-0126
G Kargl ⓘ https://orcid.org/0000-0001-9125-0256

References

Carrier W D, Olhoeft G R and Mendell W 1991 Physical properties of the lunar surface *Lunar Sourcebook* ed Heiken G H, Vaniman D T and French B M (Cambridge: Cambridge University Press) pp 475–594

Colaprete A *et al* 2010 Detection of water in the LCROSS ejecta plume *Science* **330** 463–8

DLR Institute of Planetary Research 2021 SESAME—surface electric sounding and acoustic monitoring experiment (available at: www.dlr.de/pf/en/desktopdefault.aspx/tabid-1371/1868_read-10525/) (Accessed 20 August 2021)

Falkner P 1999 Permittivitätswellen und altimeter analysator für das ESA/NASA projekt CASSINI—HUYGENS PhD Thesis Technical University of Graz, Austria

Ferri F, Angrilli F, Bianchini G, Fulchignoni M and Team H 2002 Huygens atmospheric structure instrument of Huygens probe on Cassini mission *Acta Astronaut.* **50** 249–55

Fulchignoni M *et al* 2002 The characterisation of Titan's atmospheric physical properties by the Huygens atmospheric structure instrument (Hasi) *Space Sci. Rev.* **104** 395–431

Hayne P O, Hendrix A, Sefton-Nash E, Siegler M A, Lucey P G, Retherford K D, Williams J-P, Greenhagen B T and Paige D A 2015 Evidence for exposed water ice in the Moon's south polar

regions from Lunar Reconnaissance Orbiter ultraviolet albedo and temperature measurements *Icarus* **255** 58–69

King O, Warren T, Bowles N, Sefton-Nash E, Fisackerly R and Trautner R 2020 The Oxford 3D thermophysical model with application to PROSPECT/Luna 27 study landing sites *Planet. Space Sci.* **182** 104790

Lethuillier A, Le Gall A, Hamelin M, Schmidt W, Seidensticker K J, Grard R, Ciarletti V, Caujolle-Bert S, Fischer -H-H and Trautner R 2016 Electrical properties and porosity of the first meter of the nucleus of 67P/Churyumov-Gerasimenko *Astron. Astrophys.* **591** A32

McKay D S, Grant H, Basu A, Blanford G, Simon S, Reedy R, French B M and Papike J 1991 The lunar regolith *Lunar Sourcebook* ed G H Heiken, D T Vaniman and B M French (Cambridge: Cambridge University Press) pp 285–356

Moehlmann D, Seidensticker K, Gebhardt. W, Kochan H, Kretschmer M, Péter A, Schmidt W, Thiel K and Ziegler L 1998 Rosetta lander experiment interface document (REID-B) SESAME, RO-LSE-IF-3101

Nelson S O, 2004. Permittivity and density relationships for granular and powdered materials *IEEE Antennas and Propagation Society Symp.* (IEEE) (https://doi.org/10.1109/APS.2004.1329610)

Nurge M A 2012 *In situ* dielectric spectroscopy for water detection on the lunar surface *Planet. Space Sci.* **65** 76–82

Olhoeft G R and Strangway D W 1975 Dielectric properties of the first 100 meters of the Moon *Earth Planet. Sci. Lett.* **24** 394–404

Paige D A *et al* 2010 Diviner lunar radiometer observations of cold traps in the Moon's south polar region *Science* **330** 479–82

Petrenko V F and Whitworth R W 2002 *Physics of Ice* (Oxford : Oxford University Press) (https://doi.org/10.1093/acprof:oso/9780198518945.001.0001)

Reiss P, Warren T, Sefton-Nash E and Trautner R 2021 Dynamics of subsurface migration of water on the Moon *J. Geophys. Res.* **126**

Schorghofer N and Aharonson O 2014 The lunar thermal ice pump *Astrophys. J.* **788** 169

Seidensticker K J *et al* 2007 SESAME—an experiment of the Rosetta Lander Philae: objectives and general design *Space Sci. Rev.* **128** 301–37

Spudis P D, Bussey D B J, Baloga S M, Cahill J T S, Glaze L S, Patterson G W, Raney R K, Thompson T W, Thomson B J and Ustinov E A 2013 Evidence for water ice on the Moon: results for anomalous polar craters from the LRO mini-RF imaging radar *J. Geophys. Res.* E **118** 2016–29

Trautner R, Barber S J, Carpenter J, Fisackerly R, Houdou B, Leese M, Rusconi A, Sefton-Nash E and Zamboni A 2018 PROSPECT: a novel package for subsurface sample acquisition and analysis of lunar volatiles *Proc. 69th Int. Astronautical Congress* p IAC–18,A3,2B,2,x42773

Trautner R, Grard R and Hamelin M 2003 Detection of surface ice and water deposits on Mars with a mutual impedance probe *J. Geophys. Res.* **108** E10, 8047

Trautner R, Simões F, Grard R and Hamelin M, 2004. A new instrument for measuring the low-frequency electrical properties of planetary subsurface materials *37th ESLAB Symp. 'Tools and Technologies for Future Planetary Exploration'* p 193–6

Wenner F 1916 A method of measuring earth resistivity *Bull. Bur. Stand.* **12** 469

Zent A P, Hecht M H, Cobos D R, Campbell G S, Campbell C S, Cardell G, Foote M C, Wood S E and Mehta M 2009 Thermal and electrical conductivity probe (TECP) for Phoenix *J. Geophys. Res.* **114** E00A27

Zent A P, Hecht M H, Cobos D R, Wood S E, Hudson T L, Milkovich S M, DeFlores L P and Mellon M T 2010 Initial results from the thermal and electrical conductivity probe *J. Geophys. Res.* **115** E00E14